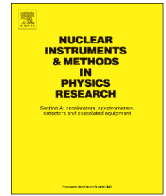




Contents lists available at ScienceDirect

Nuclear Instruments and Methods in Physics Research A

journal homepage: www.elsevier.com/locate/nima

Breakdown transient study of plasma distributions in a 2.45 GHz hydrogen discharge

O.D. Cortázar ^{a,*}, A. Megía-Macías ^b, O. Tarvainen ^c, H. Koivisto ^c^a Universidad de Castilla-La Mancha, ETSII-INEI, Applied Mechanics and Projects Department, C.J. Cela s/n, 13170 Ciudad Real, Spain^b ESS Bilbao Consortium, Polígono Ugaldeguren-III Pol. A 7B, 48170-Zamudio, Vizcaya, Spain^c University of Jyväskylä, Department of Physics, PO Box 35 (YFL), 40500 Jyväskylä, Finland

ARTICLE INFO

Article history:

Received 27 November 2014

Received in revised form

20 January 2015

Accepted 22 January 2015

Available online 4 February 2015

Keywords:

ECR ion sources

ECR plasma breakdown

Plasma diagnostics

ABSTRACT

Plasma distribution transients associated with the breakdown of a 2.45 GHz hydrogen discharge similar to high current microwave ion sources are studied by means of an ultra-fast frame image acquisition system in visible light range. Eight different plasma distributions have been studied by photographing the 2D projections of the discharge through a transparent plasma electrode. The temporal evolution of images in Balmer-alpha and Fulcher band wavelengths have been recorded associated to atomic and molecular excitation and ionization processes. Some unexpected plasma distributions transient behaviors during breakdown are reported.

© 2015 Elsevier B.V. All rights reserved.

1. Introduction

Breakdown phenomena in pulsed ECR plasma sources are of interest for many fields of physics and related instrumentation such as particle accelerators science and plasma processing industry [1,2]. Extensive research on this subject has been conducted with time resolved electrical probes, emission spectroscopy and bremsstrahlung radiation diagnostics under a wide range of parameters for different plasmas [3–5]. Understanding the plasma processes involved during the breakdown is beneficial for monocharged beam current optimization as well as the improvement of multiple charged ion production efficiency [6–8]. On the other hand, the value of ultra-fast light intensified photography in plasma dynamics research has been demonstrated by decades of experimentation in high density plasmas as Z-pinch, Exploding Wires and Plasma Foci [9–12]. Nevertheless, very few studies probing the spatial and/or temporal light emission profiles of ECR-heated plasmas have been conducted so far [13–15]. The relatively low light intensity is probably the main reason. However, considering the state of the art of MCP-CCD intensified cameras and the characteristic time scales of the breakdown dynamics in ECR plasmas, a compromise between exposure time and temporal development of the ionization cascade can be reached as is shown in this report.

Here we present an experimental study of 2.45 GHz hydrogen discharge breakdown using an ultra-fast MCP-CCD frame camera. The

present study builds upon a recent report [16] on the effect of the magnetic field topology on the observed plasma distributions and focuses on the characteristic timescale of the ignition process. This diagnostics yields information on the dynamics of excitation, ionization and dissociation processes in the volume of the plasma chamber.

2. Experimental set-up

The experimental data were taken with a 2.45 GHz microwave plasma generator TIPS (Test-bench for Ion-source Plasma Studies) [17]. The plasma was viewed through a transparent plasma electrode composed by a 10 mm thick quartz window with two grounded tungsten meshes at both sides. The window has a centered hole of 4 mm diameter for pumping.

The scheme maintains the geometry of a typical ion source plasma chamber without modifying the microwave coupling and pumping characteristics. The setup has been used previously to report the existence of the plasma distributions under study [18,16]. Fig. 1 shows a cross-sectional view of the plasma source where main parts are indicated: (a) plasma chamber, (b) microwave coupler, (c) gas inlet, (d) RF quartz window, (f) coil pancakes, (g) optical window with shielding grids, (h) vacuum tee and (i) standard quartz window placed in front of the camera. The figure includes a closeup of the transparent plasma electrode and also a normal picture of the operating system with the plasma ON just to illustrate how it looks by eye.

Fig. 2 shows the experimental schematic arrangement for the diagnostics synchronization timing. The delay between frames is

* Corresponding author.

E-mail address: daniel.cortazar@uclm.es (O.D. Cortázar).

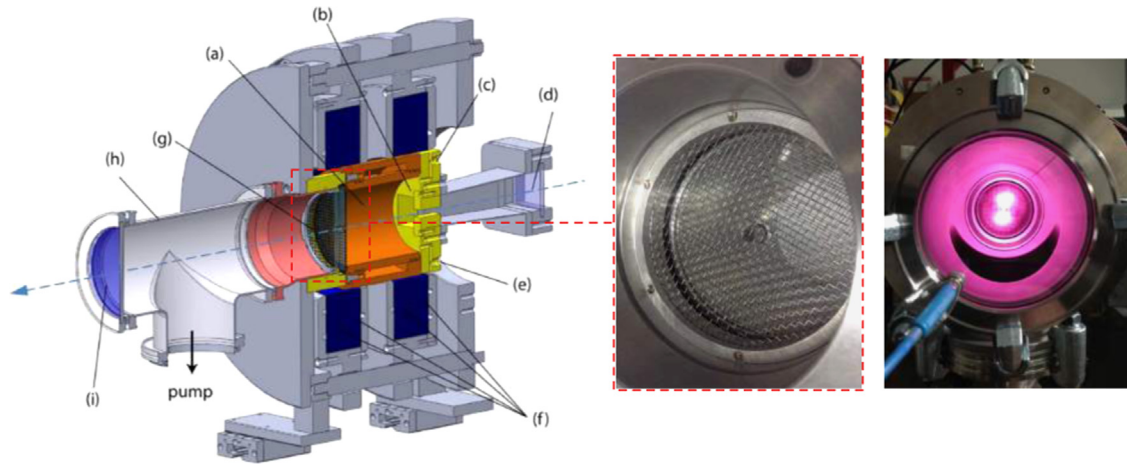


Fig. 1. Cross-sectional view of the plasma source including a transparent plasma electrode closeup picture. Also a picture with the plasma in hourglass mode is shown.

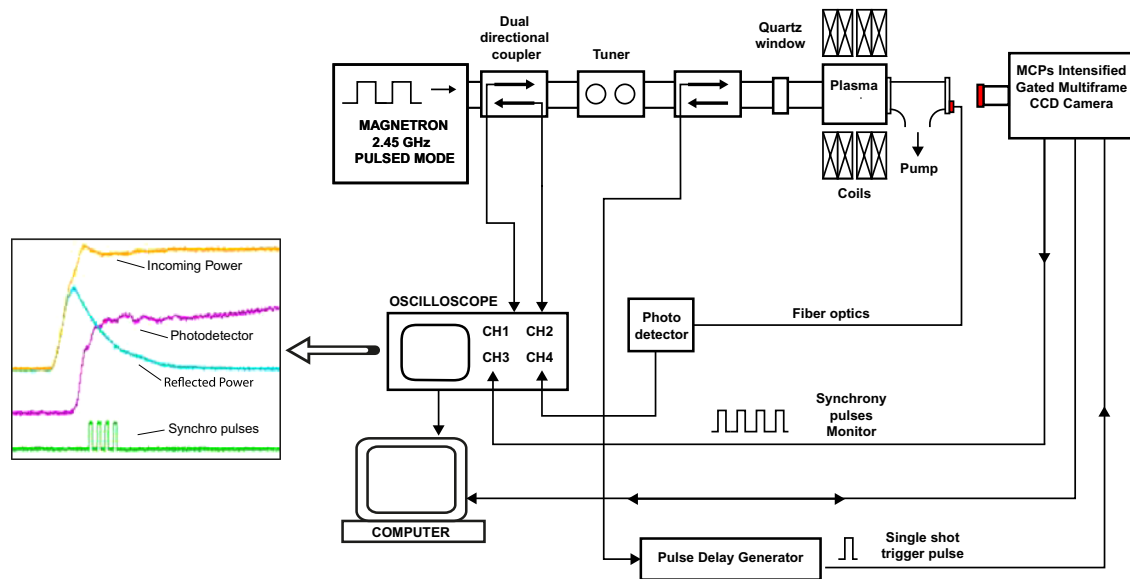


Fig. 2. Schematic representation of the experimental synchronization setup.

adjusted depending of the plasma dynamics and is referred to the rising edge of the plasma generator incident power signal. The figure also includes a typical oscilloscope record showing the measurement of incoming (P_i) and reflected (P_r) power signals with bidirectional couplers, time-resolved light emission through a fast photodiode and synchronization pulses corresponding to the pictures. These auxiliary diagnostics were used for checking the synchronism between the plasma ignition and image acquisition.

The MCP and CCD gains were adjusted depending on the light intensity to optimize the quality of the images taken through different filters. The set-up enabled us to take up to four images with independently adjusted exposure times and delays between each picture in synchronization with the hydrogen discharge breakdown. The typical exposure time used in this study was $1 \mu\text{s}$ for the high-brightness plasma distributions (*Column*, *Hourglass* and *Slug*) and $2 \mu\text{s}$ for the low-brightness ones (*Full-Chamber*, *Ring*, *Flower*, *Yin-Yang* and *Donut*).

The calibration in intensity of the images is an important issue. The camera is composed by four independent electro-optical acquisition subsystems composed by MCPs (a pair in chevron configuration), one phosphor screen and one CCD. So, each subsystem has a different intrinsic gain that not allows the use of the same settings for obtaining the same exposure degree. A matricial calibration with respect to the background was applied in order to

compensate differences between the four independent MCP-CCD sensors. In the following figures, red corresponds to the highest intensity (saturated white on black and white gamma) and blue the lowest (deep black). This set-up allowed the use of bandpass filters mounted in both the CCD camera and the photodiode in order to study monochromatic light emission in the visible range. Visible light (390–700 nm), Balmer-alpha (656.3 nm) and Fulcher band (around 600 nm) bandpass filters (Thorlabs models FB660-10 with 660 nm central wavelength and 10 nm bandpass region and FB600-40 with 600 nm central wavelength and 40 nm bandpass region) were placed inside the camera to take filtered pictures of the breakdown process. These sets of pictures can be related to the evolution of the atomic and molecular ionization processes [18,16].

3. Results

The plasma distributions observed in TIPS have been reported recently in Refs. [18,16] and can be categorized by the brightness of the visible light emission. The high-brightness distributions include *Column*, *Hourglass* and *Slug*. The low-brightness distributions are *Full-Chamber*, *Ring*, *Flower*, *Yin-Yang* and *Donut*.

Filtered pictures could only be taken in the high-brightness modes. The longer exposure time necessary to take filtered pictures in low-

brightness modes prohibits obtaining temporally well-defined images necessary for studying the evolution of the plasma distributions. Each set of pictures is divided into two groups separated by a dashed vertical line. The group on the left is obtained at the very beginning of the plasma breakdown when the corresponding intensity of light emission is relatively low. The second set of pictures on the right is obtained at later stage of the discharge when the light intensity is significantly higher. Thus, the two groups of pictures have been measured on different pulses using different MCP gains avoiding overexposure. It is of note that some of the studied plasma modes can be produced with different magnetic field profiles as demonstrated in Ref. [16]. Although the temporal characteristics of each distribution were observed to be independent of the magnetic field profile, each case under study includes the corresponding 2D magnetic maps. Therefore, only a single example of each plasma mode is discussed hereafter. The times quoted in all following figures are measured from the leading edge of the incident microwave pulse. Some of the pictures have an Halo of light surrounding the plasma structure which comes from the reflected light on the plasma chamber wall. This effect is more notorious when light intensity is higher. A white circle corresponding to plasma chamber diameter (85 mm) is added on the first picture to give the size scale. The reproducibility and pulse-to-pulse stability during the evolution of all the plasma shapes reported in this paper were observed to be high.

3.1. Column mode

Fig. 3 shows the evolution of plasma distribution during the breakdown process for the *Column* mode. The two groups of pictures (separated by a dashed line) were measured on different pulses using different MCP gains to avoid overexposed or excessively dark pictures. This fact have been taken carefully into account for the comparison of the intensities of images between the two groups.

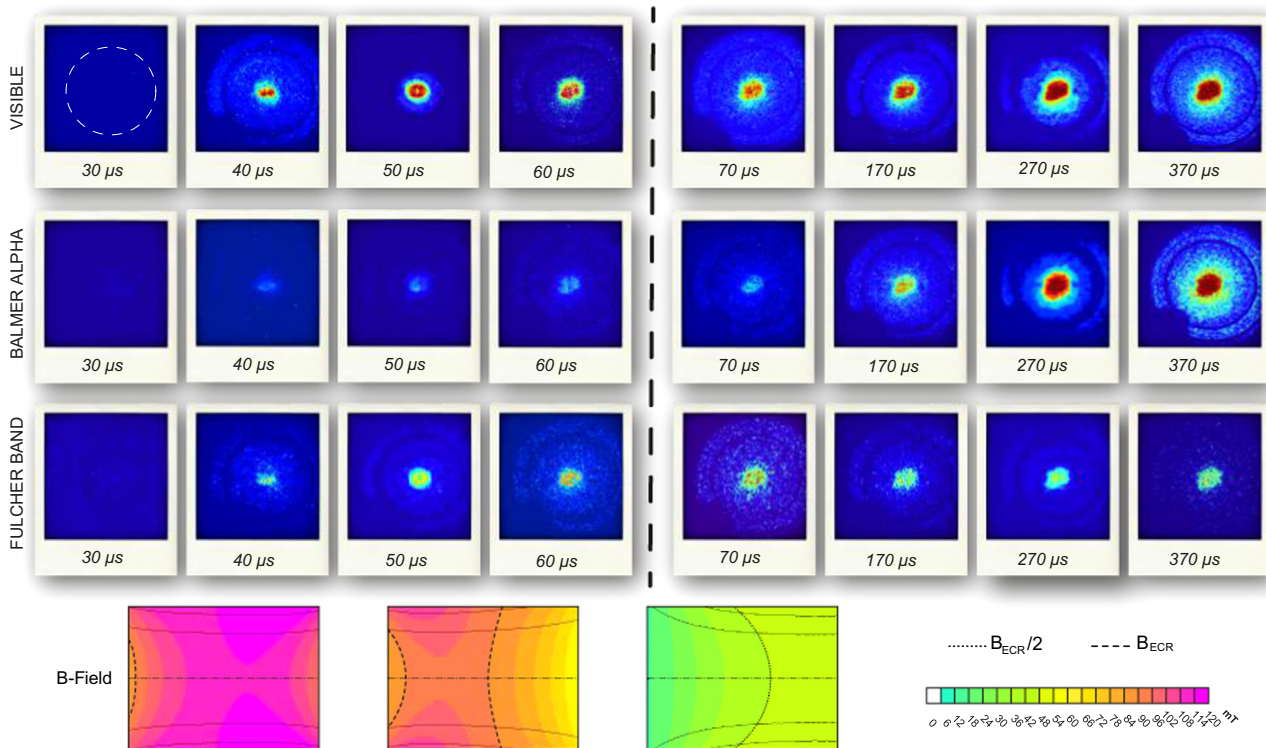


Fig. 3. *Column* normalized CCD-MCP images of visible light (1 μ s exposure time), Balmer-alpha (2 μ s) and Fulcher band (3 μ s) taken at different stages of the plasma breakdown. The corresponding operational parameters were 2100 W of incoming power at 50 Hz/10% duty factor, 3.8×10^{-3} mb neutral gas pressure. The three 2D magnetic field maps inside the plasma chamber that produce this plasma configuration are included indicating the B_{ECR} and $B_{ECR}/2$ surfaces. The superimposed white circle on the first picture has the plasma chamber diameter (85 mm) to give the scale.

The light emission profile shows that the plasma is concentrated on the chamber axis. The breakdown is initiated in a small circle that grows in diameter and reaches the steady-state distribution in 270 μ s. The Balmer-alpha emission intensity increases continuously while the Fulcher band emission exhibits a relative maximum of intensity at about 50 μ s.

3.2. Hourglass mode

Fig. 4 shows the *Hourglass* mode plasma breakdown temporal evolution. The structure starts developing from the axis of the plasma chamber showing its characteristic waist from the very beginning.

The shape grows very fast, specially in the vertical direction, reaching the final form after 80 μ s. The Fulcher band emission signal exhibits again an early intensity maximum at 30 μ s while Balmer-alpha grows monotonically until the steady-state is reached.

3.3. Slug mode

Fig. 5 shows the temporal evolution of the plasma breakdown for the *Slug* mode. The temporal evolution of the visible light exhibits a relative maximum approximately at 50 μ s and reaches saturation in 370 μ s. During the initial stage of the breakdown lasting approximately 100 μ s the Fulcher band emission is predominant with respect to the Balmer-alpha emission. Following the early temporal maximum the situation is inverted i.e. Balmer-alpha starts to dominate with the Fulcher band emission decaying slowly.

The projected view of the discharge breakdown starts from a small circular area in the center of the chamber. This circular region becomes larger in the vertical direction in 50–60 μ s. The fifth picture (70 μ s) is the first one showing clearly the stretched

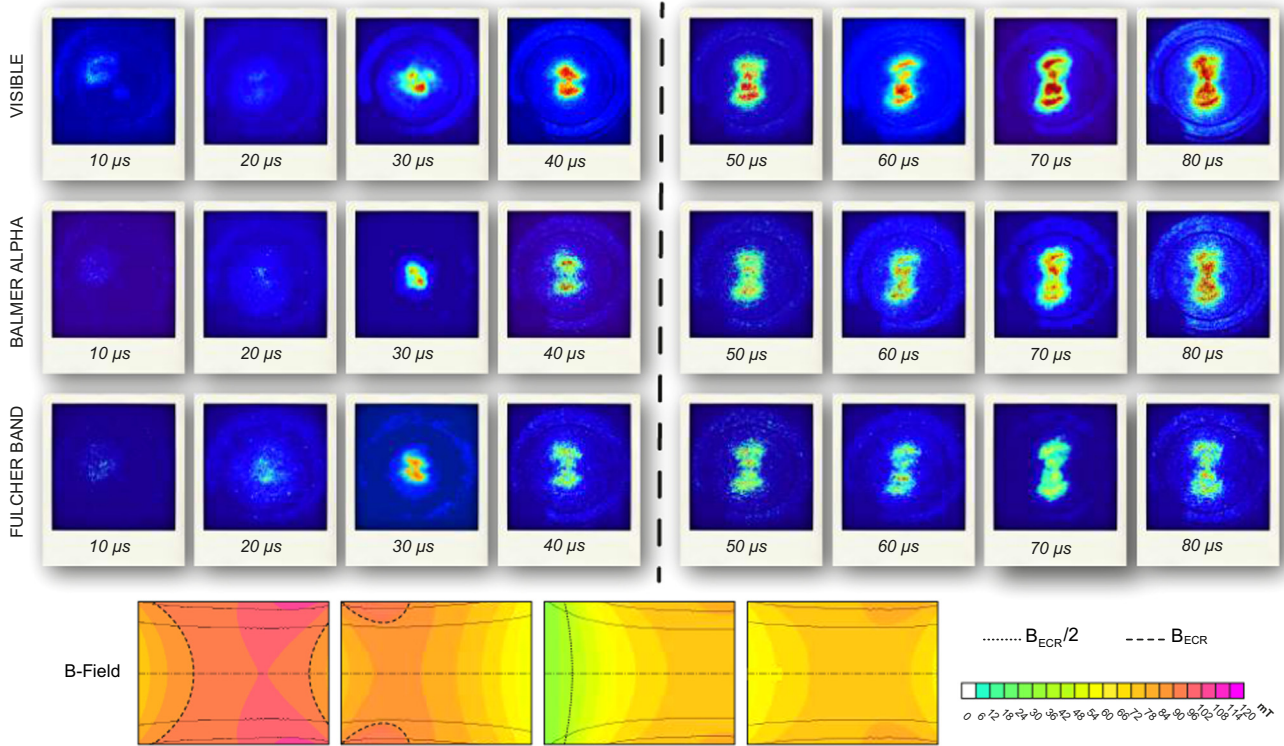


Fig. 4. Hourglass normalized CCD-MCP images of visible light ($1 \mu\text{s}$ exposure time), Balmer-alpha ($2 \mu\text{s}$ exposure time) and Fulcher band ($3 \mu\text{s}$ exposure time) taken at different stages of the plasma breakdown. The experimental conditions for this study were 2700 W input power at 50 Hz/10% duty factor, 8.6×10^{-3} mb. The four 2D magnetic field maps inside the plasma chamber that produce this plasma configuration are included indicating the B_{ECR} and $B_{\text{ECR}}/2$ surfaces.

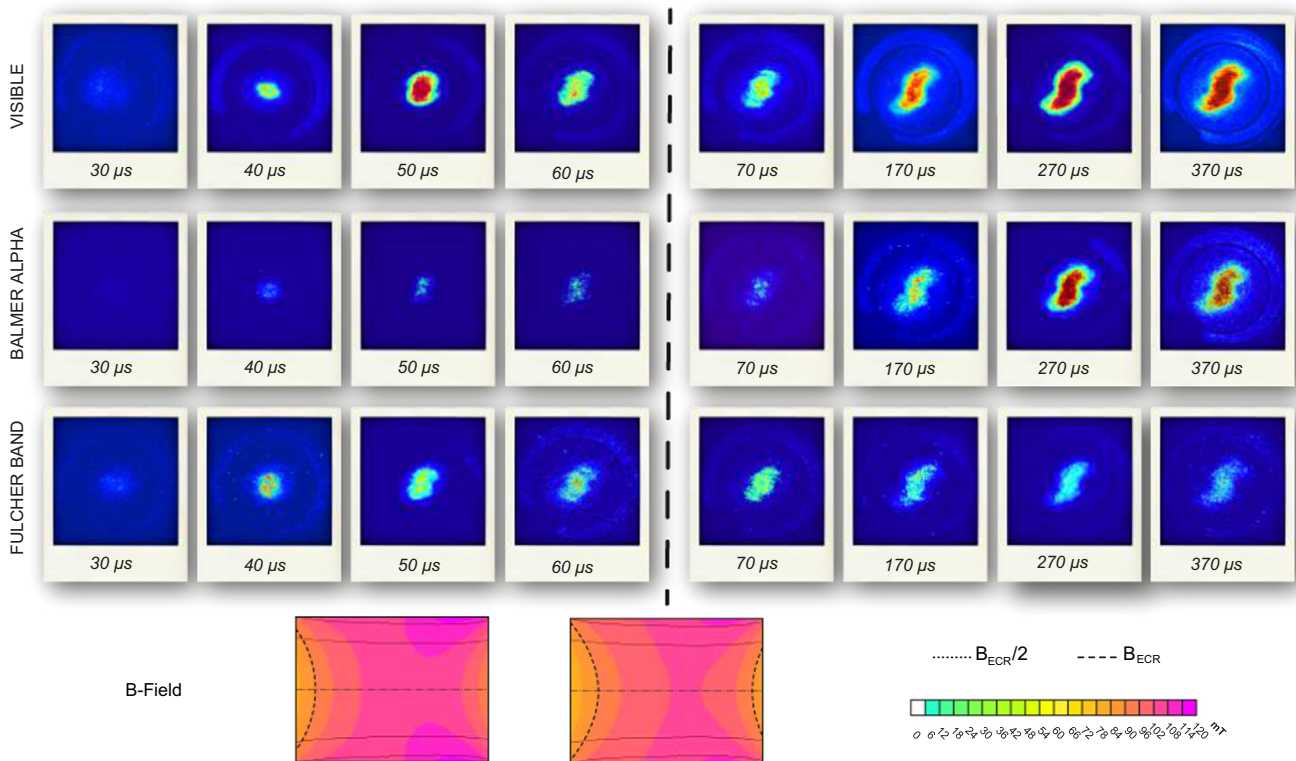


Fig. 5. Slug normalized CCD-MCP images of visible light ($1 \mu\text{s}$ exposure time), Balmer-alpha ($1 \mu\text{s}$ exposure time) and Fulcher band ($3 \mu\text{s}$ exposure time) taken at different stages of the plasma breakdown. The working conditions were set on 750 W input power at 50 Hz/10% duty factor and 3.8×10^{-3} mb hydrogen pressure. The two 2D magnetic field maps inside the plasma chamber that produce this plasma configuration are included indicating the B_{ECR} and $B_{\text{ECR}}/2$ surfaces.

'S'-like shape that characterizes the *Slug* mode. In the frame corresponding to $170 \mu\text{s}$ the final shape is already formed and in the next two pictures ($270 \mu\text{s}$ and $370 \mu\text{s}$) it gains intensity without any morphological evolution.

3.4. Flower mode

Fig. 6 shows the temporal evolution of the plasma breakdown for the *Flower* mode characterized by four lobes, two vertical ones

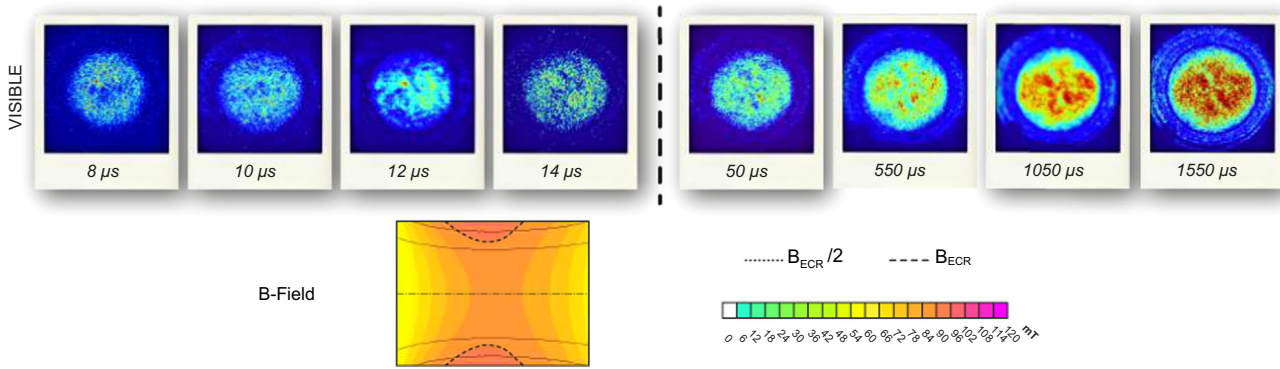


Fig. 6. Flower normalized CCD-MCP images of visible light ($2 \mu\text{s}$ exposure time) taken at different stages of the plasma breakdown. The working conditions are 1500 W input of MW power at 50 Hz/10% duty factor and 3.8×10^{-3} mb of hydrogen pressure. The 2D magnetic field map inside the plasma chamber that produces this plasma configuration is included indicating the B_{ECR} and $B_{\text{ECR}}/2$ surfaces.

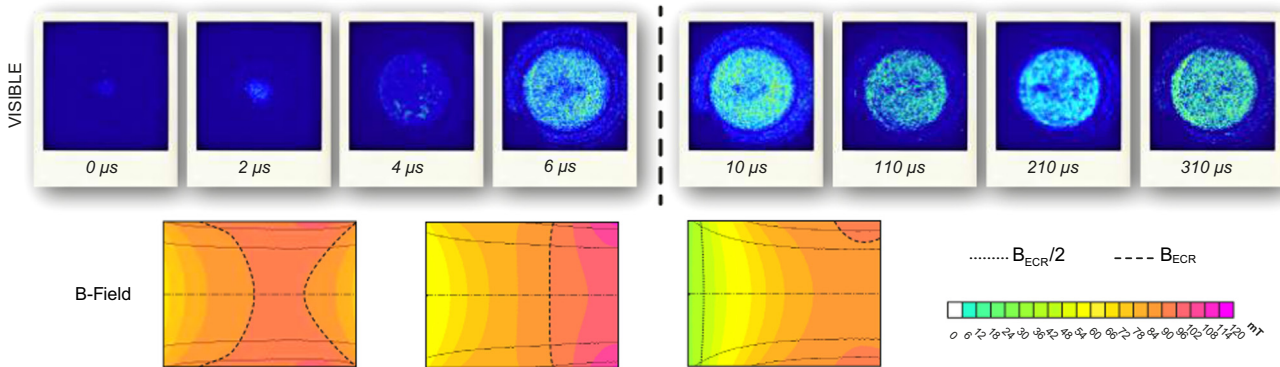


Fig. 7. Full-Chamber normalized CCD-MCP images of visible light ($2 \mu\text{s}$ exposure time) taken at different stages of the plasma breakdown. Working conditions were set at 1950 W input power at 50 Hz/10% duty factor, 3.8×10^{-3} mb of hydrogen pressure. The three 2D magnetic field maps inside the plasma chamber that produce this plasma configuration are included indicating the B_{ECR} and $B_{\text{ECR}}/2$ surfaces.

(small) and two horizontal ones (large), all of them curved counterclockwise. The intensity of light emission in the flower mode is prohibitively weak to obtain pictures through bandpass filters.

The first noticeable feature of the breakdown process is that it takes more than one 1 ms for the flower shape to be fully defined. In fact, this is the slowest breakdown process of the observed plasma distributions. The first two pictures (8 and $10 \mu\text{s}$) show a nearly homogeneous emission in the whole chamber volume with some darker areas on the axis. In frames three ($12 \mu\text{s}$) to five ($50 \mu\text{s}$), there is no well defined morphology but instead some peculiar structures appear. After a relatively long time of $500 \mu\text{s}$ the flower shape can be seen weakly in the sixth picture ($550 \mu\text{s}$). In picture number seven ($1050 \mu\text{s}$) the Flower mode is fully developed and finally in the last picture ($1550 \mu\text{s}$) an increase in the light intensity is observed.

3.5. Full-Chamber

Fig. 7 shows the temporal evolution of the plasma breakdown for the Full-Chamber mode, which is also characterized by weak light emission. The breakdown process of the Full-Chamber plasma mode is extremely fast. The final morphology is reached in approximately $6 \mu\text{s}$. The evolution starts from a small circular projection on axis that can be barely seen in the first picture. In the second picture, this shape is brighter and better defined. About $2 \mu\text{s}$ later, in the third picture, the ionization has extended to full chamber, although the light emission is very weak. Finally, from the fourth frame onward the Full-Chamber mode has completely evolved.

3.6. Ring mode

Fig. 8 shows the temporal evolution of the plasma breakdown for the Ring mode. Only visible light images are shown due to the low brightness.

The evolution of breakdown is probably the most unexpected one discussed in this report. As can be seen in the first image ($6 \mu\text{s}$), the light emission starts in two vertical lobes. Then, in the second frame ($8 \mu\text{s}$), this region grows in radial direction and becomes thinner in the middle with some structure visible close to the chamber wall. The third picture ($10 \mu\text{s}$) shows an intermediate maximum of the brightness. At the same time, the vertical part acquires an 'S'-shape and the vertical ends grow following the edge of the chamber forming four distinct lobes. In the fourth frame ($12 \mu\text{s}$), the vertical structure starts to fade while the lobes keep growing. The light emission intensity is reduced between 10 and $12 \mu\text{s}$, the fifth picture shows that the vertical structure has almost disappeared and the radial lobes have grown producing a full ring shape. The final ring configuration is reached in ($22 \mu\text{s}$).

3.7. Yin-Yang mode

Fig. 9 shows the temporal evolution of the plasma breakdown in Yin-Yang mode. As can be seen in the first picture ($5 \mu\text{s}$), the ionization starts asymmetrically out of the chamber axis. This region grows through the next four pictures and in the sixth image ($130 \mu\text{s}$) the tail of the Yin-Yang shape starts to appear. In image number seven ($230 \mu\text{s}$) the Yin-Yang shape is finally established.

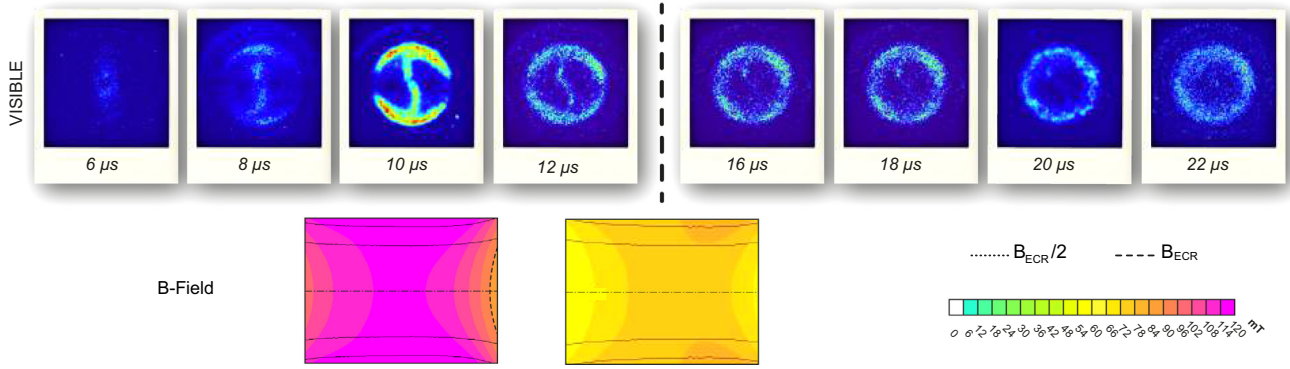


Fig. 8. Ring normalized CCD-MCP images of visible light ($2 \mu\text{s}$ exposure time) taken at different stages of the plasma breakdown. The working conditions on this study were set to 1950 W input power at 50 Hz/10% duty factor and 3.8×10^{-3} mb of hydrogen. The two 2D magnetic field maps inside the plasma chamber that produce this plasma configuration are included indicating the B_{ECR} and $B_{\text{ECR}/2}$ surfaces.

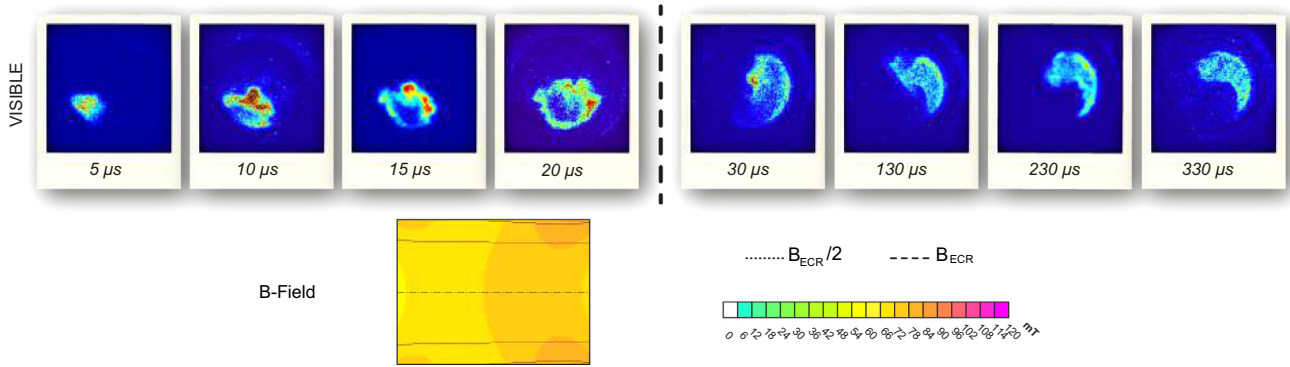


Fig. 9. Yin-Yang normalized CCD-MCP images of visible light ($2 \mu\text{s}$ exposure time) taken at different stages of the plasma breakdown. The working conditions for the study presented in this section were 1200 W input power at 50 Hz/10% duty factor and 4.3×10^{-3} mb. The 2D magnetic field map inside the plasma chamber that produces this plasma configuration is included indicating the B_{ECR} and $B_{\text{ECR}/2}$ surfaces.

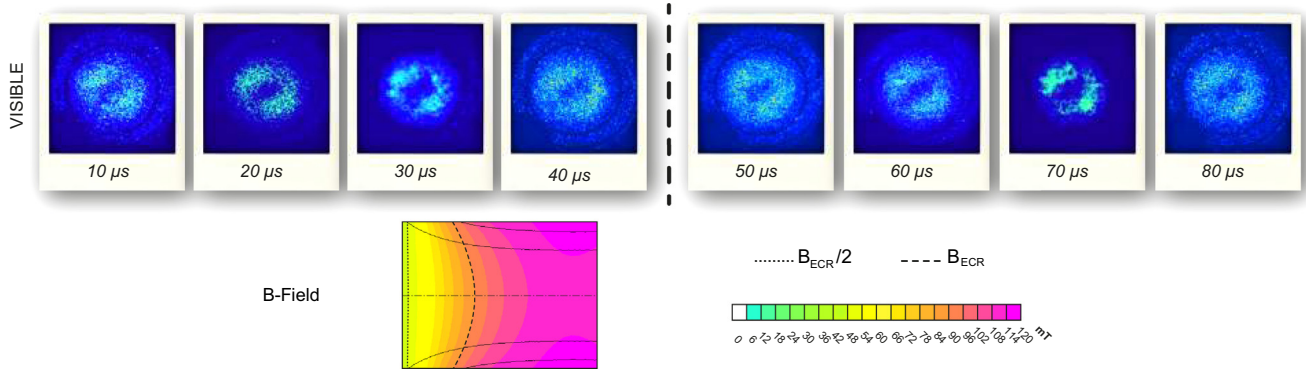


Fig. 10. Donut normalized CCD-MCP images of visible light ($3 \mu\text{s}$ exposure time) taken at different stages of the plasma breakdown. The working conditions in this experiment were set to 2100 W input power at 50 Hz/10% duty factor and 8.6×10^{-3} mb hydrogen pressure. The 2D magnetic field map inside the plasma chamber that produces this plasma configuration is included indicating the B_{ECR} and $B_{\text{ECR}/2}$ surfaces.

3.8. Donut mode

Fig. 10 shows the temporal evolution of the plasma breakdown in Donut mode. The low-brightness of this plasma distribution mode makes impossible to obtain pictures before $10 \mu\text{s}$. This structure starts from the beginning with its characteristic annular shape.

4. Summary and conclusions

Here we have reported an experimental study on the transient effects of plasma distributions in a 2.45 GHz ECR hydrogen plasma source during the breakdown of the discharge. Sets of ultra-fast

pictures for visible light, Balmer- α and Fulcher band obtained during single pulses are presented. The images give information about the temporal and spatial evolution of molecular and atomic excitation.

Although the range of evolution times is broad, the behavior of Balmer-alpha and Fulcher band emissions are similar for all the cases. Fig. 11 shows the typical normalized photodiode signals of light emissions: Visible, Balmer- α and Fulcher band obtained during the entire pulse duration [16]. Saturation time for Balmer- α and time when Fulcher band reaches its maximum value are indicated. While the Balmer-alpha emission grows slowly, the Fulcher band emission always presents a peak at the very beginning of the breakdown process followed by a slow decay. The maximum of the Fulcher-band emission implies the molecular dissociation rate

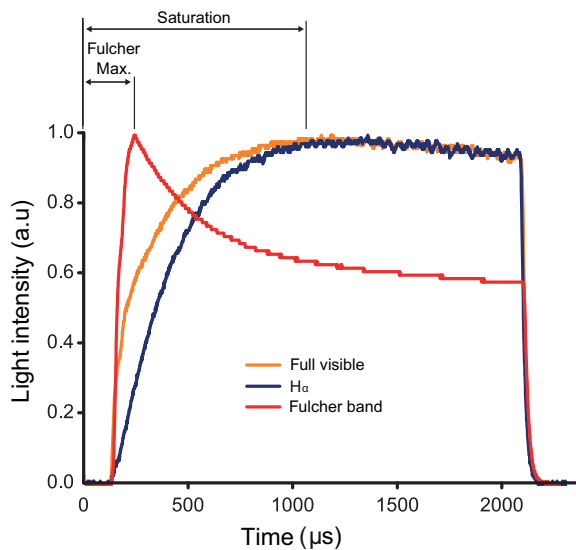


Fig. 11. Typical photodiode signals for visible, Balmer- α and Fulcher band where Balmer- α saturation time and Fulcher band maximum time are indicated.

Table 1
Summary of characteristic evolution times and experimental conditions.

Plasma Distribution Modes	Balmer- α sat. (μ s)	Fulcher max. (μ s)	P_i (W)	$(P_i - P_r)/P_i$ (%)	Gas pressure $\times 10^{-3}$ (mb)
Column	370	50	2700	60	3.8
Hourglass	80	30	2700	50	8.6
Slug	370	50	750	70	3.8
Flower	1500	12	1500	40	3.8
Full-Chamber	300	10	1950	35	3.8
Ring	22	10	1950	30	3.8
Yin-Yang	330	15	1200	10	4.3
Donut	80	20	2100	40	8.6

through triplet state excitation peaks at the beginning of the plasma breakdown. The peak could be due to favorable electron energy distribution and/or varying density of neutral molecules.

Table 1 lists Balmer- α saturation time, transient peak time for the maximum of Fulcher band emission, incoming power, absorbed percentage of power and neutral gas pressure recorded during the experiments to facilitate an overview. The evolution of the high light intensity modes recorded by the camera are coincident with the photodiode records but for the low intensity cases the characteristic times were obtained only from the photodiode signals. Considering the well defined peak in the Fulcher band signals (as is shown in Fig. 11) the error for these measurements can be established in less than 5% while in the saturation time the estimation of the error to reach the 100% of the maximum intensity value is above 10%.

The agreement between light emission evolutions observed in the picture sequences with the photodiode signals shown in Fig. 11 (at least in the high intensity cases) suggests a possible relationship with recent results of ion species composition obtained on a similar plasma source [19]. In that study it has been shown that the temporal evolution of the species fraction ($H^+/H_2^+/H_3^+$) of the extracted ion beams exhibits similar characteristics with the Balmer- α and Fulcher-band emissions discussed here. The development of diagnostic device combining an extraction system, Wien filter and optical emission spectroscopy is being prepared to study the relationship between the ion ratios with visible light emissions for plasma distributions.

Acknowledgments

The authors would like to thank to Dr. Javier Bermejo and Dr. Joan Bordas for their continued support during the experiments.

References

- [1] S. Gammino, L. Celona, G. Ciavola, F. Maimone, D. Mascali, *Review of Scientific Instruments* 81 (2010) 02B313.
- [2] J. Pelletier, A. Anders, *IEEE Transactions on Plasma Sciences* 33 (6) (2005) 1944.
- [3] O. Cortázar, A. Megía-Macías, A. Vizcaíno-de Julián, *Review of Scientific Instruments* 83 (10) (2012) 3302.
- [4] T. Fujimoto, S. Miyachi, K. Sawada, *Nuclear Fusion* 28 (7) (1988) 1255.
- [5] T. Ropponen, O. Tarvainen, I. Izotov, J. Noland, V. Toivanen, D. Machicoane, G. Leitner, H. Koivisto, T. Kalvas, O. Peura, P. Jones, V. Skalyga, V. Zorin, *Plasma Sources Science and Technology* 20 (2011) 055007.
- [6] O. Tarvainen, T. Ropponen, V. Toivanen, J. Árje, H. Koivisto, *Plasma Sources Science and Technology* 18 (2009) 035018.
- [7] H. Bäcker, J.W. Bradley, P.J. Kelly, R.D. Arnell, *Journal of Physics D: Applied Physics* 34 (2001) 2709.
- [8] C. Lyneis, J. Benítez, D. Leitner, J. Noland, M. Strohmeier, H. Koivisto, O. Tarvainen, Characterization of the microwave coupling to the plasma chamber of the lbl ecr ion source, in: *Proceedings of ECRIS 2010, Grenoble, France, 2010*, pp. 162–164.
- [9] F.C. Gibson, M.L. Bowser, C.W. Ramaley, F.H. Scott, *Review of Scientific Instruments* 25 (1) (1954) 73.
- [10] J.O. Pouzo, M.M. Milanese, O.D. Cortázar, R. Moroso, Images of the dense plasma focus phenomenon in the 2-kJ PACO device, *IEEE Transactions on Plasma Sciences* 33 (2) (2005).
- [11] O.D. Cortázar, A.R. Piriz, G.R. Prieto, D.H.H. Hoffmann, N.A. Tahir, Preliminary results of a 10 kJ Z-pinch, *AIP Conference Proceedings* 996 (1), 2008.
- [12] M.M. Milanese, O.D. Cortázar, R. Moroso, J. Nieldbaski, L. Supán, The plasma focus current sheath in a squirrel cage gun, *IEEE Transactions on Plasma Sciences* 39 (11) (2011).
- [13] R. Racz, S. Biri, J. Palanikas, *Plasma Sources Science and Technology* 20 (2011) 025002.
- [14] S. Biri, R. Racz, J. Palanikas, Studies of the ecr plasma in the visible light range, in: *Proceedings of ECRIS 2010, Grenoble, France, 2010*.
- [15] N. Nishino, Y. Nakashima, Y. Higashizono, S. Kobashashi, K. ISLAM, Y. Kubota, M. Yoshikawa, Y. Mishima, T. Cho, *Plasma and Fusion Research* 1 (2006) 035.
- [16] O.D. Cortázar, A. Megía-Macías, O. Tarvainen, A. Vizcaíno-de Julián, H. Koivisto, *Plasma Sources Science and Technology* 23 (2014) 065028.
- [17] A. Megía-Macías, O.D. Cortázar, A. Vizcaíno-de Julián, *Review of Scientific Instruments* 85 (3) (2014) 033310.
- [18] O. Cortázar, A. Megía-Macías, A. Vizcaíno-de Julián, O. Tarvainen, J. Komppula, H. Koivisto, *Review of Scientific Instruments* 85 (2) (2014) 02A902.
- [19] Y. Xu, S. Peng, H. Ren, J. Zhao, J. Chen, T. Zhang, A. Zhang, Z. Guo, J. Chen, *Review of Scientific Instruments* 79 (2) (2008) 02B713.